Support Information

Enhanced Photocatalytic Hydrogen Evolution by Polyiodide-Boosted Electron Transport and Pt-Ag Alloy Active Sites in Conductive Polymer-Based Core-Shell Photocatalysts

Wenyan Zhang[a,], Chaoqun Jiang[b], Weidong Tao[a], Yihan Wang[a] Hangmin Guan[a], Lingyun Hao[a]*

[a]College of Material Engineering, Jinling Institute of technology, Nanjing 211169, China

[b]College of Architecture Engineering, Jinling Institute of technology, Nanjing 211169, China

[*]Corresponding author: E-mail: wiseyanyan@jit.edu.cn Tel.: +86-25-86188966. Fax: +86-25-86188966

1. XRD and XPS analysis

The formation of Pt–Ag alloy nanodots and the associated electronic interaction between Pt and Ag were further confirmed by XRD and C 1s XPS analyses. The XRD pattern of the Fe_3O_4@PPy@Pt/Ag@I sample is presented in Fig. S1. Distinct diffraction peaks corresponding to Pt–Ag alloys (expected near 40° for the (111) plane of a cubic phase) are not clearly observable. This absence could be attributed to the small size and high dispersion of the Pt-Ag alloy nanodots, as shown in TEM images (Fig. 1(c,d).). According to the Scherrer equation, nanocrystals with sizes of approximately 3 nm would generate significantly broadened diffraction peaks that merge into the background, resulting in weak alloy-related signals compared with the dominant reflections of the Fe_3O_4 core.

Fig. S2(a) and Fig. S2(b) shows the C 1s XPS spectra of Fe_3O_4@PPy@Ag@I and Fe_3O_4@PPy@Pt/Ag@I sample. The evolution of the C 1s spectra provides additional insight into the interfacial charge interaction between the alloy nanodots and the PPy matrix. In both samples, the dominant C 1s peak at 284.8 eV (C–C/C–H) remains unchanged, confirming reliable binding energy calibration. Notably, Fe_3O_4@PPy@Pt/Ag@I exhibits a pronounced enhancement of the component at approximately 287.7 eV relative to Fe_3O_4@PPy@Ag@I. This feature is typically

assigned to oxidized or highly polarized carbon species (C–N^+/polaron) within PPy, indicating an increased degree of polymer oxidation. Such enhancement suggests that the in situ formation of Pt–Ag alloy nanodots promotes interfacial electron transfer from the PPy backbone to the bimetallic nanoparticles, resulting in a higher p-doping level of the PPy shell.

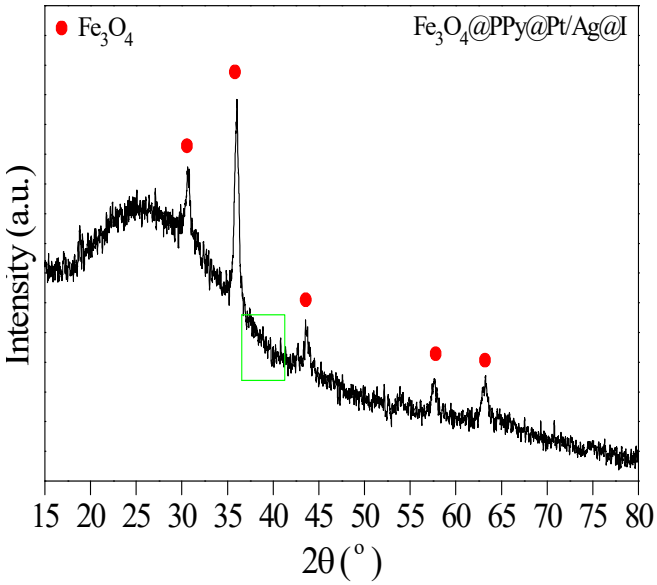

Fig. S1 XRD pattern of the Fe_3O_4@PPy@Pt/Ag@I photocatalyst

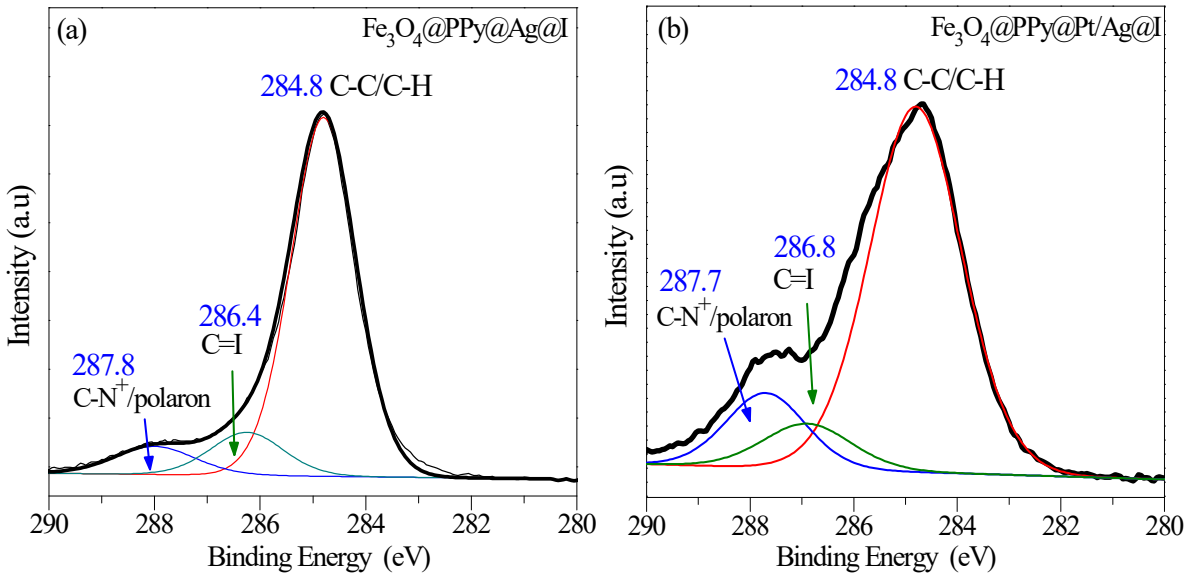

Fig. S2 C 1s XPS spectra of (a) Fe_3O_4@PPy@Ag@I and (b) Fe_3O_4@PPy@Pt/Ag@I

2. Calculation of Pt-based Mass Activity of photocatalysts and analysis

The Pt mass-specific activity was calculated using the formula:

*Mass Activity (μmol h^{-1} mg^{-1} Pt) = (Hydrogen Evolution (μmol g^{-1}) *10^{-3}) / Time (h)*

The mass of Pt in the catalysts was determined based on the nominal loading from the synthesis precursors. The calculated mass activity is summarized in Tab. S1.

Tab. S1 Mass activity of photocatalysts

Photocatalyst	**Hydrogen Evolution** (μmol g^{-1} Pt)	**Pt mass activity** (μmol h^{-1}·g^{-1} Pt)
Fe_3O_4@PPy@Pt	55349	27674.5
Fe_3O_4@PPy@Pt/Ag@I	344279	172139.5

The results shown in Tab. S1 demonstrating reduced noble-metal dependency. The `$Fe_3O_4$@PPy@Pt/Ag@I` catalyst exhibits a significantly higher Pt mass activity (172 μmol·h^{-1}·mg^{-1} Pt) compared to Fe_3O_4@PPy@Pt` (27.7` μmol·h^{-1}·mg^{-1} Pt). This finding confirms that the superior performance of our optimized catalyst is not due to a higher usage of the precious Pt metal, but rather stems from a genuine enhancement in the intrinsic activity of the catalytic sites. The results suggest that forming Pt-Ag alloys effectively maximizes the utility of every atom of the precious platinum metal., contributingg to This enhancement can be attributed to the synergistic effects of Pt-Ag alloying, including:

(1) Electronic modulation of Pt via charge transfer from Ag, optimizing the binding energy of reaction intermediates.

(2) Improved charge separation and transfer within the alloy nanostructure.

(3) The LSPR effect of Ag enhancing light harvesting and potentially generating hot electrons that contribute to the reaction.

3. Raman analysis

The Raman spectra of the samples are shown in Fig. S3, providing insights into

the successful coating and interfacial electronic interactions within the composites. The Fe_3O_4@Pt sample exhibits characteristic D and G bands at approximately 1328 and 1554 cm^{-1}, respectively, which could be related to residual carbonaceous species.

For Fe_3O_4@PPy@Ag@I, a pronounced attenuation of carbon-related Raman signals is observed, indicating that the PPy matrix forms a continuous overlayer that effectively shields the underlying carbon species from laser excitation. Meanwhile, the residual D and G bands exhibit systematic blue shifts accompanied by peak broadening (G band: 1554 → 1560 cm^{-1}; D band: 1328 → 1345 cm^{-1}). Such spectral evolution is commonly associated with charge-transfer interactions and p-type doping effects in conjugated carbon-containing systems, where electron density withdrawal leads to increased vibrational frequencies.

In the present system, these Raman features are consistent with electronic interactions between the polyiodide-doped PPy matrix and the carbon-containing interfacial layer, suggesting that polyiodide species may modulate the local electronic structure through electron-accepting behavior.

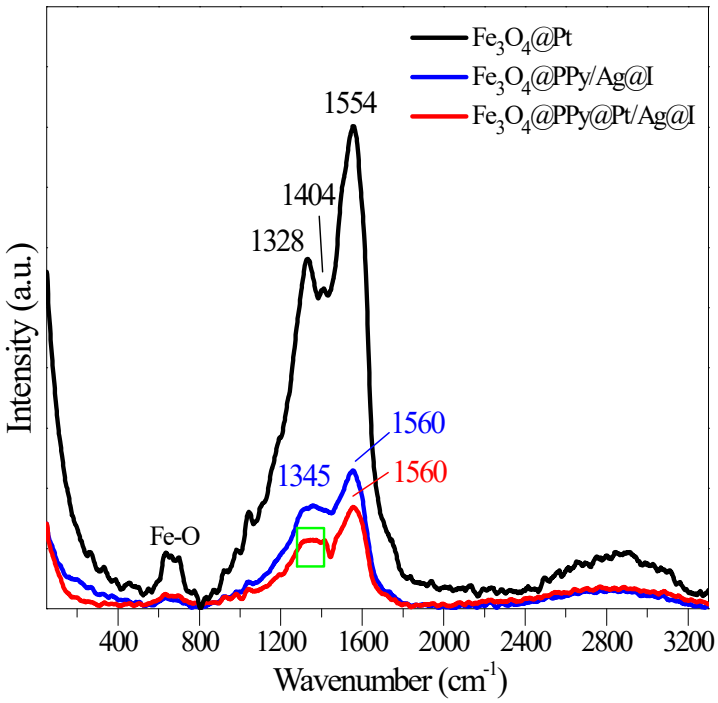

Fig. S3 Raman spectra of Fe_3O_4@Pt, Fe_3O_4@PPy@Ag@I and Fe_3O_4@PPy@Pt/Ag@I

For Fe_3O_4@PPy@Pt/Ag@It, the further attenuation and broadening of the

carbon-related Raman bands indicate a more complex interfacial environment. This behavior can be reasonably associated with the introduction of Pt–Ag alloy nanoparticles, which provide additional pathways for interfacial charge transfer. The polyiodide-containing PPy matrix is likely to facilitate this process by serving as an electron-transport medium between the polymer framework and the metallic active sites.

Taken together with the observation of C–N^+ species in the XPS spectra (Fig. S2), the Raman results support the presence of polyiodide-associated p-type electronic modulation in the PPy-based composite, although these spectroscopic features should be regarded as indirect evidence of doping and interfacial charge-transfer effects.

4. FTIR analysis

The FTIR spectra of Fe_3O_4@PPy@Ag@I and Fe_3O_4@PPy@Pt/Ag@I are very similar (Fig. S4), indicating that the chemical backbone of the PPy matrix remains intact during the subsequent photodeposition of Pt. This observation suggests that the alloy formation does not disrupt the primary polymer structure.

Compared with Fe_3O_4@PPy@Ag@I, the Fe_3O_4@PPy@Pt/Ag@I composite exhibits enhanced absorption in the 1011–765 cm^{-1} region, which is assigned to C–H out-of-plane bending vibrations of PPy, along with the emergence of a new band at approximately 849 cm^{-1}. These spectral changes suggest a modification of the polymer chain conformation, which is often associated with increased planarity and ordering in doped conjugated polymers.

Because both samples contain polyiodide species, the additional changes observed after Pt–Ag alloy formation are plausibly related to altered polymer–metal and polymer–dopant interactions rather than changes in chemical composition. Such conformational adjustments are known to facilitate charge delocalization in conductive polymers.

Therefore, although FTIR spectroscopy does not directly probe charge carriers, the observed structural evolution of the PPy matrix is consistent with enhanced

electronic coupling between the polyiodide-doped polymer network and the Pt–Ag alloy active sites, which may contribute to improved charge transport and photocatalytic performance.

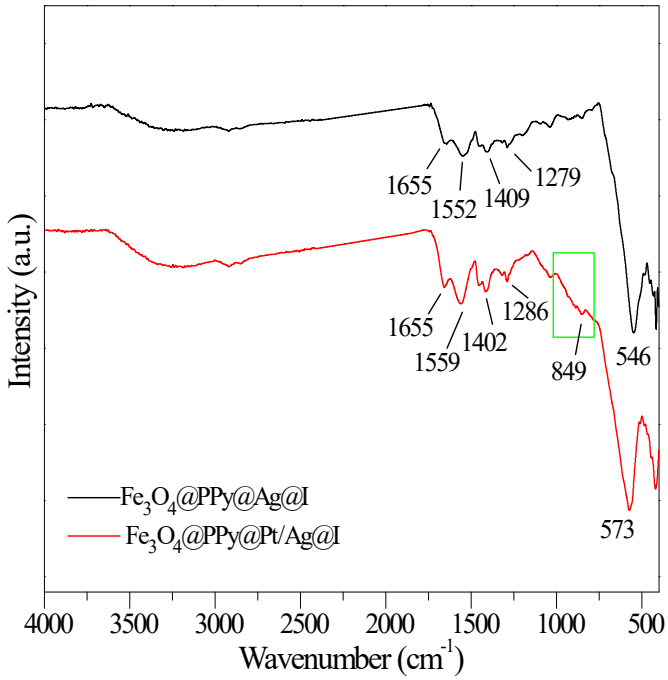

Fig. S4 FTIR spectra of Fe_3O_4@PPy@Ag@I and Fe_3O_4@PPy@Pt/Ag@I

5. Stability testing of the optimized photocatalyst

An extended stability test was conducted over a total duration of 24 hours, consisting of eight consecutive photocatalytic cycles, followed by post-reaction characterization. As shown in Fig. S5, the optimized Fe_3O_4@PPy@Pt/Ag@I photocatalyst exhibits stable hydrogen evolution activity during the initial operation period, with each cycle lasting 3 h. After prolonged irradiation, a gradual attenuation in activity is observed, reflecting typical long-term operational behavior of polymer-based photocatalytic systems.

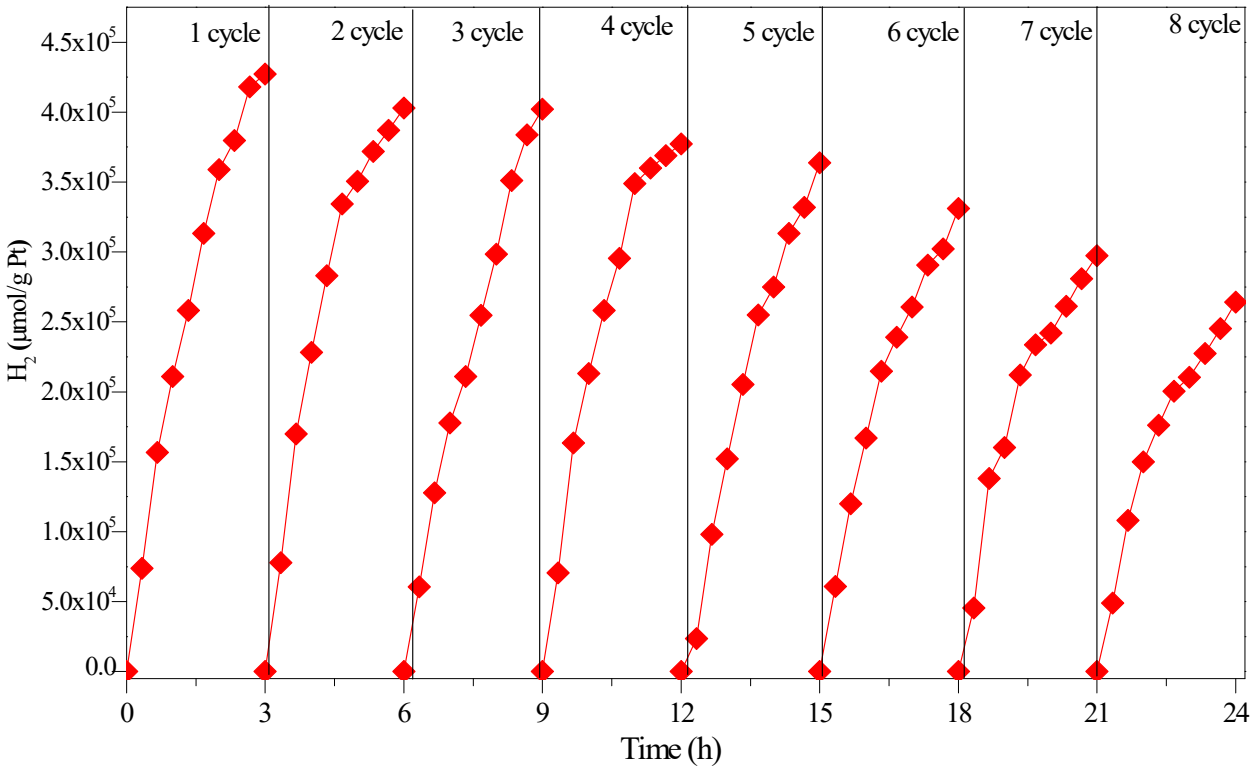

Fig. S5 Cycling stability of Fe_3O_4@PPy@Pt/Ag@I for photocatalytic hydrogen evolution over 24 h, consisting of eight consecutive cycles (3 h per cycle)

To assess the chemical stability of the photocatalyst, Fourier transform infrared (FTIR) spectroscopy was performed after 24 h of continuous photocatalytic operation. As presented in Fig. S6, all characteristic vibrational bands associated with the PPy backbone are well preserved, indicating that no irreversible chemical degradation of the polymer framework occurs during prolonged visible-light irradiation.

Compared with the pristine Fe_3O_4@PPy@Pt/Ag@I sample prior to reaction (Fig. S4), only minor spectral variations are detected after long-term operation, including a slight decrease in the intensity of the band at approximately 849 cm^{-1}. Such spectral evolution suggests a partial relaxation of the highly ordered and doped PPy conformation under sustained photocatalytic conditions, rather than chemical decomposition of the polymer.

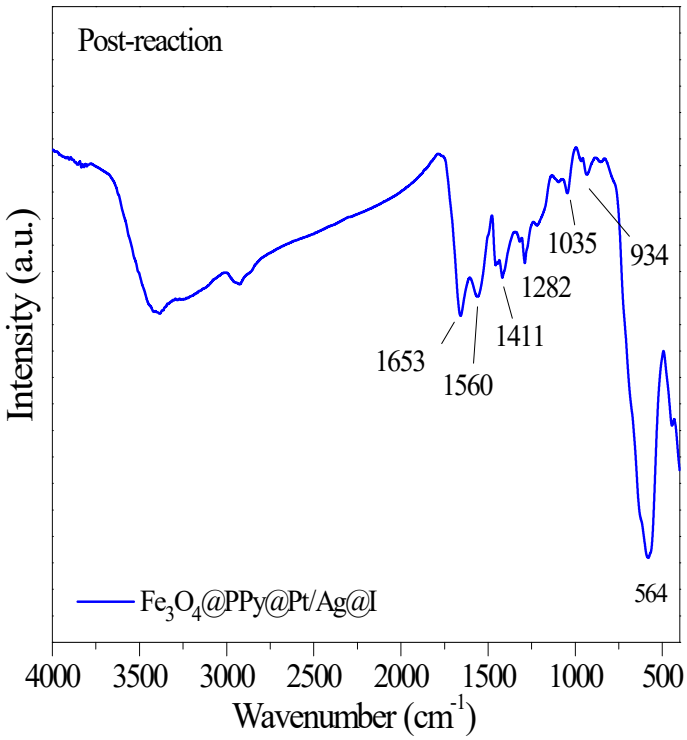

Fig. S6 FTIR spectrum of Fe_3O_4@PPy@Pt/Ag@I after eight photocatalytic cycles (24 h total duration)

This interpretation is further corroborated by post-reaction TEM observations (Fig. S7), which reveal partial fragmentation and deformation of the core–shell microstructure after extended cycling. These morphological changes are indicative of accumulated physical and mechanical stress arising from continuous hydrogen bubble evolution, polymer chain relaxation, and interfacial strain within the core–shell architecture. Importantly, the combined FTIR and TEM analyses demonstrate that the observed activity decay predominantly originates from physical and structural evolution, rather than irreversible chemical degradation or loss of catalytically active components.

From a sustainability perspective, this behavior represents a realistic operational degradation pathway commonly encountered in polymer-based photocatalysts. The insights gained here highlight potential routes for further optimization, such as mechanical reinforcement of the polymer shell, enhanced crosslinking, or structural stabilization strategies, to improve long-term durability.

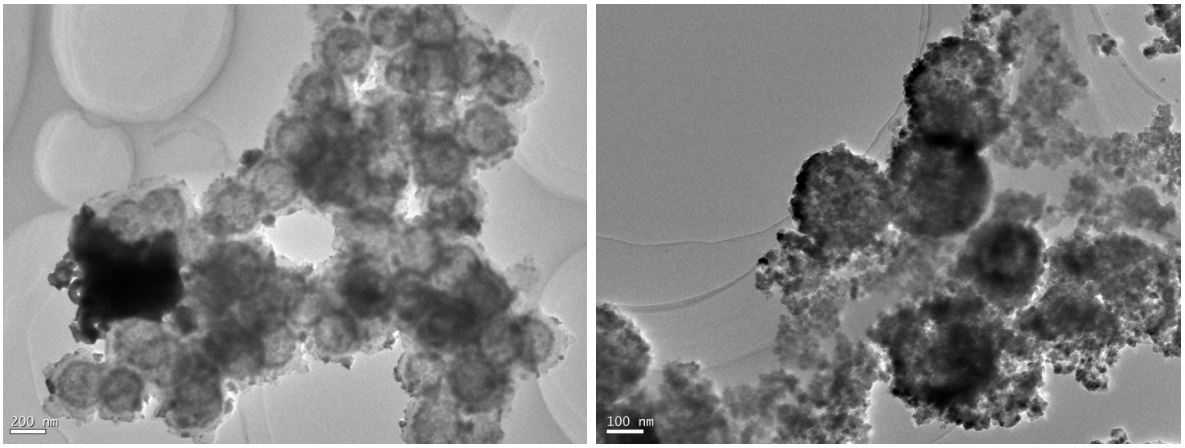

Fig. S7. TEM images of Fe_3O_4@PPy@Pt/Ag@I after 24 h of photocatalytic stability testing (eight consecutive cycles).

6. Morphology of Fe_3O_4@Pt photocatalyst

Fig. S8 shows that the Fe_3O_4@Pt photocatalyst exhibits a well-defined microspherical morphology. Each Fe_3O_4 microsphere is observably composed of aggregated Fe_3O_4 nanocrystals with a rough and textured surface. This hierarchical structure provides abundant anchoring sites, which are favorable for the high dispersion and stable immobilization of Pt species on the Fe_3O_4 surface.

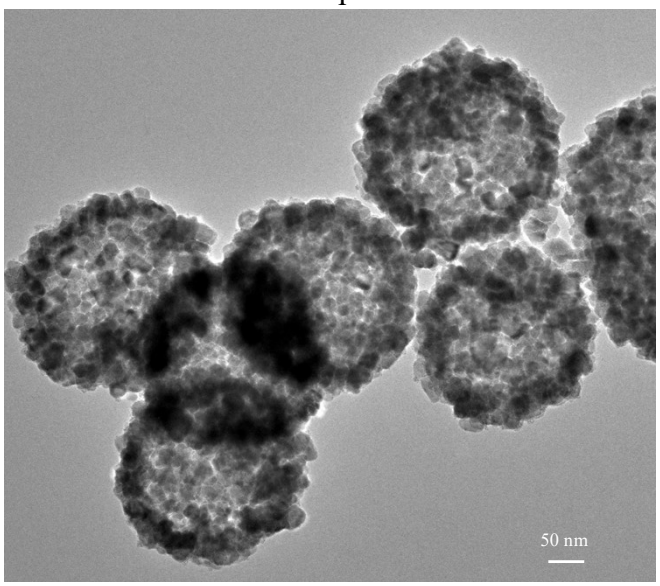

Fig. S8 TEM image of the Fe_3O_4@Pt photocatalyst

7. Benchmark comparison of photocatalytic hydrogen evolution performance

Fig. S9 presents the photocatalytic HER activities of different photocatalyst. The Fe_3O_4@PPy@Pt/Ag@I exhibits superior activity compared with Fe_3O_4@PPy@Pt,

Fe_3O_4@PPy@Pt/Ni and Fe_3O_4@PPy@Pt/Co. These results demonstrates that the exceptional performance of Fe_3O_4@PPy@Pt/Ag@I catalyst is not solely attributed to the formation of Pt–Ag alloys, which intrinsically modulate the electronic structure of Pt, but is further promoted by iodine-enhanced interfacial charge transfer.

Furthermore, as summarized in Tab. S2, the HER rate of Fe_3O_4@PPy@Pt/Ag@I is significantly higher than that of many recently reported composite photocatalysts, including noble-metal-based systems (e.g., Au–RGO/N–RGO–TiO_2), MOF-derived structures (e.g., $Cd_{0.5}Mn_{0.5}ZnS$/ZIF-8), and polymer-based photocatalysts (e.g., Pt/CBM/PF3T). In addition, the AQY of 12.5% enables Fe_3O_4@PPy@Pt/Ag@I to outperform many reported counterparts, highlighting its high efficiency in visible-light utilization. Moreover, the extended stability test further indicates the practical durability of the Fe_3O_4@PPy@Pt/Ag@I photocatalyst.

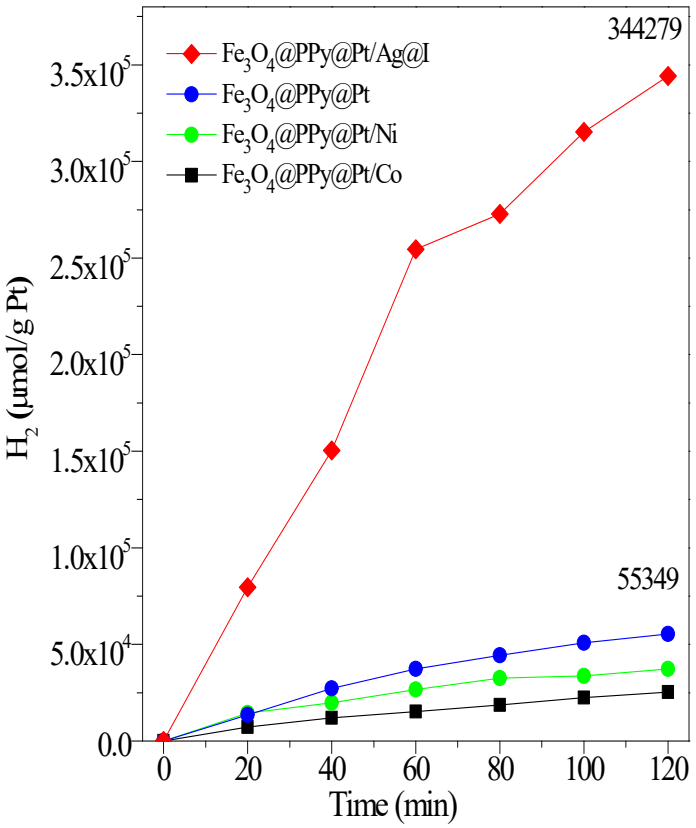

Fig. S9 Comparison of photocatalytic H_2 evolution rates of Fe_3O_4@PPy@Pt/Ag@I, Fe_3O_4@PPy@Pt, Fe_3O_4@PPy@Pt/Ni, and Fe_3O_4@PPy@Pt/Co

Tab. S2 Benchmark comparison of representative conductive polymer–based and Pt-containing photocatalysts for HER

Note: Values are provided for contextual comparison only; experimental conditions and normalization methods vary among studies. Most literature values are normalized by total catalyst mass, whereas Pt mass activity in this work is calculated based on nominal Pt loading. Some HER rates and AQY values are reported under different irradiation conditions and normalization methods, and are listed here for qualitative benchmarking only.

Photocatalyst (Key Composition)	Maximum HER Rate	Apparent Quantum Yield (AQY)	Stability (Cycles/Duration)	Ref
Fe_3O_4@PPy@Pt/Ag@I	172139.5 (μmol h^{-1}·g^{-1} Pt)	AQY 12.5% (at 420 nm)	8 cycle/24 h	This work
Au-RGO/N-RGO-TiO_2	525 μmol h^{-1} g^{-1}	Maximum AQY 2.46%	3 cycle/12 h	[S1]
$Cd_{0.05}Mn_{0.05}Zn_{0.90}$(ZIF-8)	3300 μmol h^{-1} g^{-1}	Maximum AQY 8.16%	4 cycle/16 h	[S2]
Pt- g-C_3N_4-(Au/TiO_2)	1520 μmol h^{-1} g^{-1}	AQY 7.5% (at 400 nm)	3 cycle/15 h	[S3]
PdAg/g-C_3N_4	3430 μmol h^{-1} g^{-1}	8.43% (at 420nm)	7 cycle/28 h	[S4]
Ag@$CoFe_2O_4$/g-C_3N_4	335 μmol h^{-1} g^{-1}	3.35% (at 420nm)	4 cycle/16 h	[S5]
Pt/PCBM/PF3T	70 μmol h^{-1} g^{-1}	AQY 2.0% (at 460nm)	——	[S6]
Pt (sub-2 nm)/twinned $Zn_{0.5}Cd_{0.5}S$	164.9 μmol h^{-1} (as reported)	8.56% (at 420nm)	5 cycle/30 h	[S7]
Pt/M (M=Rh, Au, Ag, Cu)/TpBpy COFs	800 μmol in a 1.5 h interval	AQY 12.8% at 450nm	6 cycle/9h	[S8]
Pt/Ni@NiO/Mg:$SrTiO_x$	60 μmol g^{-1} min^{-1}	AQY 10% at 300-400nm	——	[S9]
FeNi@NGC/g-C_3N_4 (FNC15)	167 μmol h^{-1} g^{-1}	7.28% (at 420nm)	4 cycle/20 h	[S10]

Reference

[S1] P. A. Bharad, K. Sivaranjani, C. S. Gopinath. A rational approach towards enhancing solar water splitting: a case study of Au-RGO/N-RGO-TiO_2. Nanoscale 2015, 7, 11206-11215.

[S2] S. D. Kshirsagar, S. P. Shelake, H. Islam, S. Bhattacharyya, M. Ahmadipour, A. V. Sesha Sainath, U. Pal. In situ decoration of $Cd_{0.05}Mn_{0.05}Zn_{0.90}$(ZIF-8) photocatalyst for solar-driven hydrogen production. Int. J. Hydrogen Energy 2025, 137, 1260-1268.

[S3] P. Devaraji, C. S. Gopinath. Pt-g-C_3N_4- (Au/TiO_2): Electronically integrated nanocomposite for solar hydrogen generation. Int. J. Hydrogen Energy 2018, 43(2), 601-613.

[S4] N. Xiao, Y. Li, S. Li, X. Li, Y. Gao, L. Ge, G. Lu. In-situ synthesis of PdAg/g-C_3N_4 composite photocatalyst for highly efficient photocatalytic H_2 generation under visible light irradiation. Int. J. Hydrogen Energy 2019, 44(36), 19929-19941.

[S5] S. Bellamkonda, C. Chakma, S. Guru, B. Neppolian, G. Ranga Rao. Rational design of plasmonic Ag@$CoFe_2O_4$/g-C_3N_4 p-n heterojunction photocatalysts for efficient overall water splitting. Int. J. Hydrogen Energy 2022, 47(43), 18708-18724.

[S6] L. Y. Ting, Y. I. A. Reyes, B. H. Li, M. H. Elsayed, J. C. W. Chan, J. Jayakumar, C. L. Chang, W. C. Lin, Y. J. Lu, C. Coluccini, H. Y. T. Chen, H. H. Chou. Mechanistic Understanding of Visible-Light-Driven Hydrogen Evolution on Pt Sites in Organic Nanohybrids Enhanced with Hydroxyl Additives. ACS Appl. Energy Mater. 2022, 5, 7, 7950-7955.

[S7] B. J. Ng, L. K. P. Putri, X. Y. Kong, K. P. Y. Shak, P. Pasbakhsh, S. P. Chai, A. R. Mohamed. Sub-2 nm Pt-decorated $Zn_{0.5}Cd_{0.5}S$ nanocrystals with twin-induced homojunctions for efficient visible-light-driven photocatalytic H_2 evolution. Appl. Catal. B: Environ. 2018, 224, 360-367.

[S8] L. Zhang, H. Zhang, H. Hang, L. Gao, Y. Wu, Z. Zhao, L. Niu, Y. Li. Engineering interface charge transfer between COFs and Pt cocatalyst for enhanced photocatalytic performance. Appl. Surf. Sci. 2025, 704, 163474.

[S9] K. Han, Y. C. Lin, C. M. Yang, R. Jong, G. Mul, B. Mei. Promoting Photocatalytic Overall Water Splitting by Controlled Magnesium Incorporation in $SrTiO_3$ Photocatalysts. ChemSusChem 2017, 10(22), 4568-4576.

[S10] S. Chen, X. Zhou, J. Liao, S. Yang, X. Zhou, Q. Gao, S. Zhang, Y. Fang, X. Zhong, S. Zhang. FeNi intermetallic compound nanoparticles wrapped with N-doped graphitized carbon: a novel cocatalyst for boosting photocatalytic hydrogen evolution. J. Mater. Chem. A 2020, 8, 3481-3490.